Supporting Information:

Binding and Orientation of Carbamate Pesticides on Silica Surfaces

Leander Bromley III,[a§] *Pablo E. Videla,*[b§] *Jerry L. Cartagena-Brigantty,*[a]

Victor S. Batista,[b*] *Luis Velarde*[a*]

[a] *Department of Chemistry, University at Buffalo, State University of New York, Buffalo, New York 14260-3000, United States*

[b] *Department of Chemistry, Yale University, New Haven, Connecticut 06520, United States*

[§] L.B. and P.E.V. contributed equally to this work.

Corresponding Authors

*Email: victor.batista@yale.edu; lvelarde@buffalo.edu;

Table of Content

Carbaryl IR and Raman Spectra

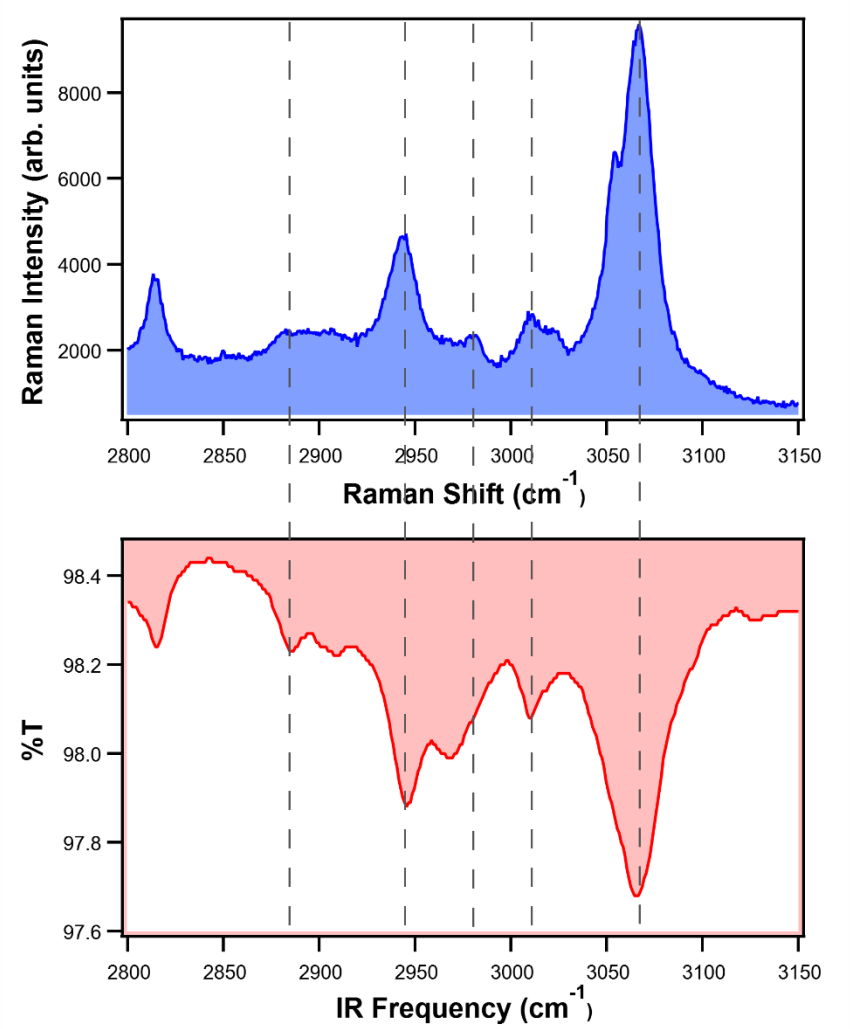

Figure S1. Powder Raman (top panel) and IR (bottom panel) spectra of carbaryl. Dashed lines are guides for the eye and represent the peaks discussed in the manuscript.

Concentration-dependent VSFG

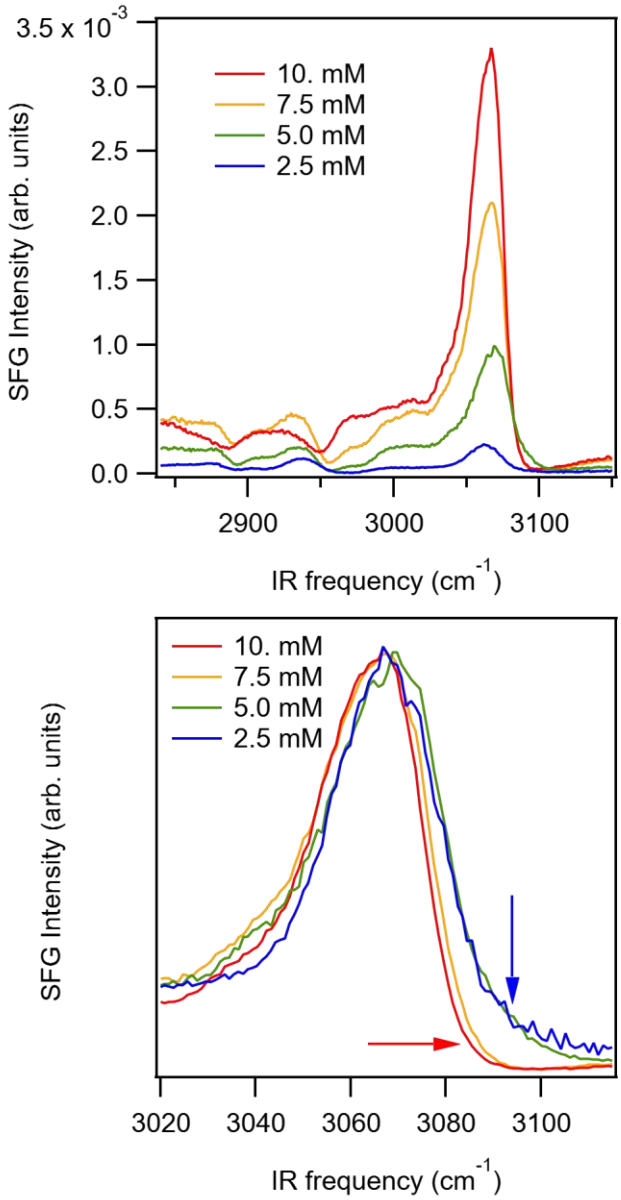

Figure S2. SSP VSFG spectra from carbaryl on silica prepared by spin-coating from acetonitrile solutions at different concentrations (top panel). The lineshape changes for the 7.5 mM and 10 mM (red arrow, bottom panel) are noticeable compared to the 2.5 mM and 5 mM (blue arrow, bottom panel) when the spectra are normalized to the aromatic CH. It is interesting to notice that in the higher concentration films, the aromatic CH grows significantly more than any of the other contributions. The higher concentration films were also prone to slow photodegradation during the experiment.

Internal Heterodyned Phase Resolved (IHPR) SFG

Phase-resolved vSFG. Right-handed z-cut α crystalline quartz has been commonly used as an external local oscillator to obtain vSFG spectral phase information due to its distinct crystalline properties. The non-linear crystal has a 3-fold azimuthal angle spectral phase dependence due to its D_3 symmetry. Another advantageous characteristic of quartz crystal is that it is spectroscopically flat. In summary, when the vSFG spectrum of a sample deposited onto the z-cut α crystal quartz surface is measured, the vSFG response has contributions from the bulk of the z-cut α quartz crystal and the molecules adsorbed on the quartz crystal surface. As a result, the SFG spectrum intensity (*I*), may be directly measured, as follows:

$$I \propto \left|\vec{\chi}^{(2)}_{S,eff}\right|^2 = \left|\vec{\chi}^{(2)}_{S,Re} + i\vec{\chi}^{(2)}_{S,Im} + i\vec{\chi}^{(2)}_{Quartz}\right|^2$$
$$= \left|\vec{\chi}^{(2)}_{Quartz}\right|^2 + 2\vec{\chi}^{(2)}_{Quartz} \cdot \vec{\chi}^{(2)}_{S,Im} + \left|\vec{\chi}^{(2)}_{S}\right|^2 \qquad \text{(S1)}$$

where $\vec{\chi}^{(2)}_{S,eff}$, is the effective non-linear susceptibility of the surface, $\vec{\chi}^{(2)}_{S,Re}$ and $i\vec{\chi}^{(2)}_{S,Im}$are the real and imaginary components of the sample, respectively, and $i\vec{\chi}^{(2)}_{Quartz}$ is the non-linear response of the quartz crystal. The $i\vec{\chi}^{(2)}_{Quartz}$ term is non-resonant, so the overall SFG spectra is a direct measurement of the (absorptive) imaginary phase spectra.

A detailed phase-resolved SFG study by Wang et. al showed the application of the internal-heterodyne method by utilizing the azimuthal angle phase dependence of the right-handed z-cut α quartz crystal.[1, 2] In our experiment, carbaryl SSP and PPP spectra on quartz were obtained at azimuthal angles of Φ=0° (+x axis) and Φ=180° (-x axis); two azimuthal angles at which $\vec{\chi}^{(2)}_{Quartz}$ is at a maximum under SSP and PPP polarization conditions. At Φ=0°, $\vec{\chi}^{(2)}_{Quartz}$ is defined as having a positive phase while it is defined to have a negative phase at Φ=180°. In contrast, the phase values of $\vec{\chi}^{(2)}_{S,Im}$ at both Φ=0° and Φ=180° remain unchanged and dictated by the sample. Therefore, the cross term changes its sign, allowing for a clear determination of the absolute phase of the molecular dipole at the surface. An expression for the quartz-normalized SFG intensity at a particular frequency, ω, in a heterodyne-detected SFG-VS experiment:

$$I^{Norm}_{\pm x}(\omega) = \frac{\left|\chi^{(2)}_{eff,\pm x}\right|^2}{\left|\chi^{(2)}_{Quartz,+x}\right|^2} = 1 \pm 2 \cdot \frac{\chi^{(2)}_{Im}}{\chi^{(2)}_{Quartz}} + \frac{\left|\chi^{(2)}_{S}\right|^2}{\left|\chi^{(2)}_{Quartz,+x}\right|^2} \qquad \text{(S2)}$$

We recorded $I_{\pm x}^{Norm}$ spectra (or $I_{0°}^{Norm}$ and $I_{180°}^{Norm}$) by a 15 second acquisition and normalized to non-resonant response of the bare z-cut α quartz crystal under the +x direction (see the SI). From equation (S3), the normalized imaginary component reported here can be obtained therefore via:

$$\frac{\chi_{S,Im}^{(2)}}{\chi_{Quartz,+x}^{(2)}} = \frac{I_{+x}^{Norm} - I_{-x}^{Norm}}{4} \quad (3)$$

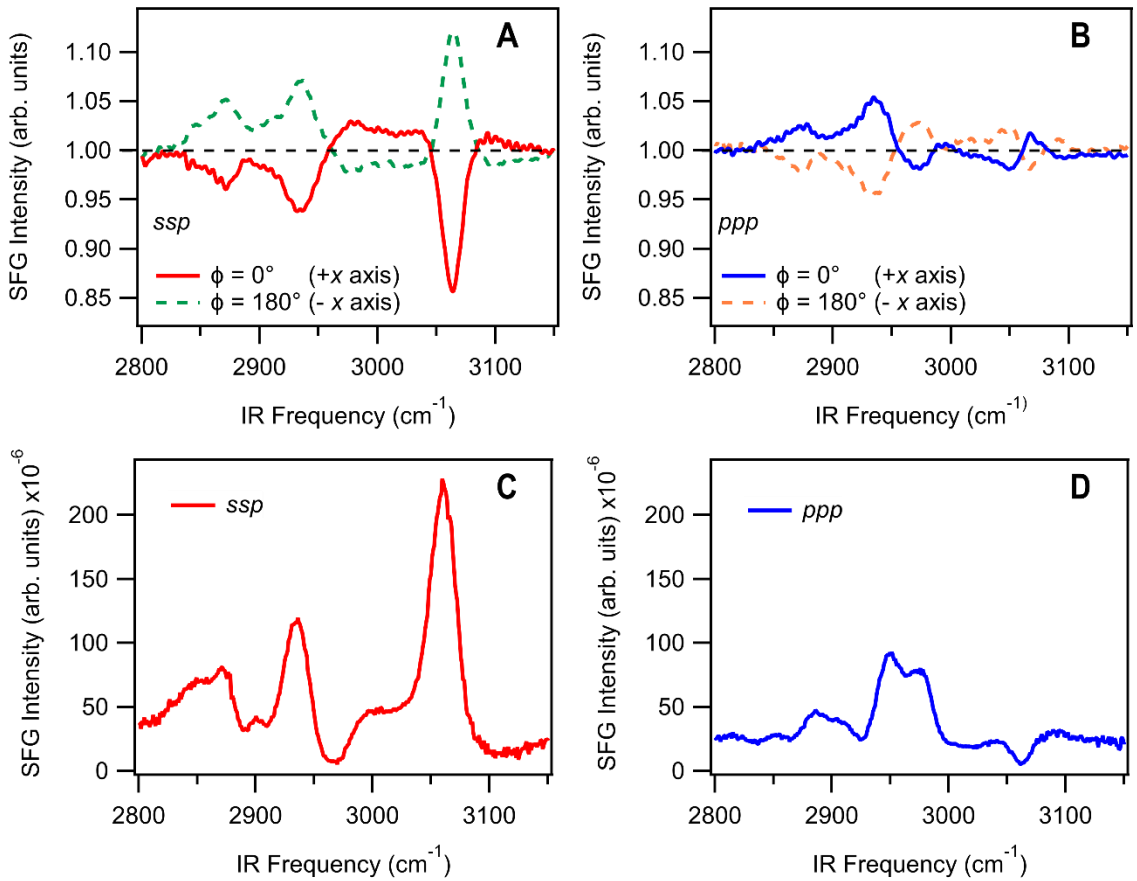

Figure S3. IHPR vSFG spectra of carbaryl on z-cut α-quartz crystal surface in ssp (A) and ppp (B) polarizations with azimuthal orientation of ϕ = 0 and 180° as indicated. The spectra are normalized to the intensity at ϕ = 0° of bare z-cut quartz, so the baseline equals to unity. The intensity spectra on the lower panels are the vSFG spectra of carbaryl on an amorphous quartz surface.

Spectral Fitting Parameters

Table S1. Parameters obtained from global fitting of SSP and PPP spectra as described in the text.

Phase-resolved SFG				
	A_{SSP}	A_{PPP}	ω	Γ
$Re\{\chi^{(2)}_{NR}\}$	_	_	_	_
$Im\{\chi^{(2)}_{NR}\}$	-0.0013+/-0.0002	-0.0054 +/- 0.0005	_	_
Peak 1	-0.049 +/- 0.007	0.022 +/- 0.004	2848.09 +/- 0.66	8.69 +/- 1.18
Peak 2	-0.230 +/- 0.009	0.126 +/- 0.006	**2870.70 +/- 0.20**	11.88 +/- 0.43
Peak 3	-0.804 +/- 0.037	0.651 +/- 0.051	**2936.26 +/- 0.20**	19.32 +/- 0.46
Peak 4	1.304 +/- 1.121	-4.633 +/- 4.483	**2975.72 +/- 5.62**	41.24 +/- 6.42
Peak 5	-1.084 +/- 1.426	10.44 +/- 6.460	2999.25 +/- 11.36	48.57 +/- 7.35
Peak 6	0.253 +/- 0.513	-4.484 +/- 6.900	**3008.26 +/- 3.56**	34.71 +/- 7.66
Peak 7	5.624 +/- 7.72	-3.547 +/- 3.688	**3061.74 +/- 1.88**	23.09 +/- 3.30
Peak 8	-6.7827 +/- 7.888	2.70552 +/- 3.796	**3063.8 +/- 1.11**	18.79 +/- 2.49
Peak 9	1.238 +/- 1.757	-0.034 +/- 0.462	3070.76 +/- 3.98	19.55 +/- 1.40

Homodyne SFG				
	A_{SSP}	A_{PPP}	ω	Γ
$Re\{\chi^{(2)}_{NR}\}$	0.0044 +/- 0.0001	0.0050 +/- 0.0001	_	_
$Im\{\chi^{(2)}_{NR}\}$	-0.0027 +- 0.0002	-0.0003 +/- 0.0003	_	_
Peak 1	-0.035 +/- 0.006	0.011 +/- 0.002	2853.83 +/- 0.66	13.59 +/- 0.53
Peak 2	-0.091 +/- 0.006	0.031 +/- 0.003	**2878.94 +/- 0.27**	13.00 +/- 0.73
Peak 3	-0.314 +/- 0.046	0.125 +/- 0.019	**2937.30 +/- 0.32**	17.45 +/- 0.77
Peak 4	0.508 +/- 0.059	-0.270 +/- 0.023	2943.29 +/- 3.03	48.82 +/- 6.16
Peak 5	0.039 +/- 0.005	-0.034 +/- 0.003	**2984.55 +/- 0.43**	11.11 +/- 0.63
Peak 6	0.455 +/- 3.242	-0.009 +/- 0.544	**3055.08 +/- 6.59**	17.60 +/- 5.35
Peak 7	-0.337 +/- 3.24	-0.128 +/- 0.556	**3056.40 +/- 4.43**	15.99 +/- 7.94
Peak 8	-0.204 +/- 0.044	0.154 +/- 0.019	3067.31 +/- 0.58	15.865 +/- 0.62

Molecular Dynamic Simulations

MD simulations were performed for carbaryl on a model slab of amorphous silica. The silica slab used is based on previous studies,[3, 4] and corresponds to a 115×115×20 Å slab adopted from the work of Cruz et al.[5] Our model of the silica surface had a surface Si−OH concentration of 4/nm^2, within the experimental range of 2.6–4.6/nm^2.[6] The exact concentration of carbaryl adsorbates onto the silica surface is not known. We have assumed a dilute surface concentration of 0.1/nm^2 for the MD simulations. This corresponds to a total of 13 carbaryl molecules on the model slab of amorphous silica surface. **Figure S4** shows a representative configuration of the simulated system.

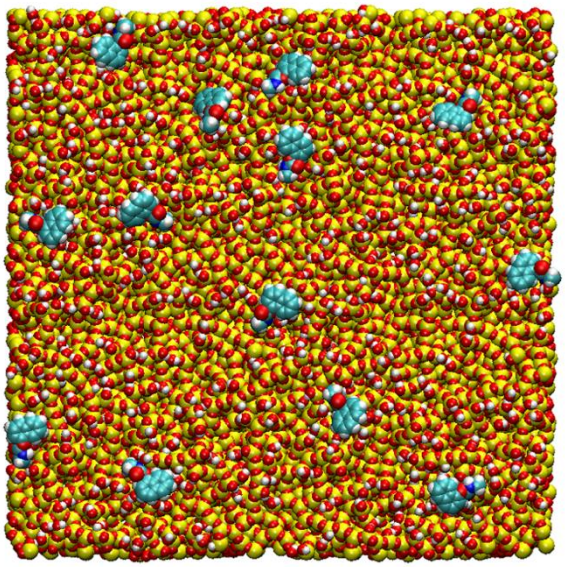

Figure S4. Typical configuration of the MD simulation.

The interaction parameters for the amorphous silica were taken from Ref.[5] The force field parameters have been optimized to reproduce the water contact angle and have been successfully applied to simulate amorphous silica surfaces,[7] quartz(1011)−water interfaces,[8] and ionic transport in silica channels.[9] The initial force field parameters for the carbaryl molecules were generated via the MATCH web server,[10] based on the CGenFF engine.[11-13] The atomic charges were obtained from the fitted restricted electrostatic potential (RESP) based on DFT calculations at the B3LYP/6-31+G(d) level of theory.[14-16] **Table S2** and **Table S3**. summarize the parameters.

Table S2. Carbaryl atom charges for the various atom types (based on CGenFF[10-12]) in carbaryl.

Atom name	Atom type	Charge (e)
C1	C261	0.062710
C2	C261	0.117349
C3	C261	-0.211384
O1	O301	-0.384840
C4	C2O6	0.629939
O2	O2D1	-0.514297
N1	N2S1	-0.335766
H1	HGP1	0.227247
C5	C331	-0.146645
H2	HGA3	0.094543
H3	HGA3	0.094543
H4	HGA3	0.094543
C6	C261	0.220611
C7	C261	-0.139773
C8	C261	-0.222297
H5	HG61	0.135569
C9	C261	-0.113413
H6	HG61	0.168455
C10	C261	-0.151070
C11	C261	-0.163400
H7	HG61	0.155567
C12	C261	-0.150881
H8	HG61	0.134191
H9	HG61	0.125949
H10	HG61	0.134714
H11	HG61	0.137836

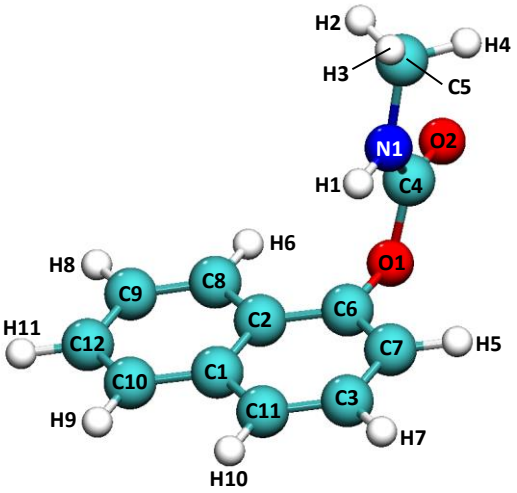

Table S3. Silica intermolecular parameters based on the CWCA force field. [4]

Atom	Charge (e)	ε (kcal/mol)	r_{min} (Å)
Si	0.90	0.3000	4.2950
O_b	-0.45	0.1500	2.5000
O_h	-0.66	0.1521	3.5400
H	0.43	0.0460	0.4490

All MD simulations were carried out using the NAMD program.[17] The carbamate molecules were randomly positioned on the hydroxylated surface using the Packmol package,[18] and the entire system was minimized for 15000 steps. The whole system was then equilibrated for 100 ps before

launching a production run of 20 ns and recording the configuration snapshots every 1 ps. Simulations were performed with an integration time step of 1 fs and periodic boundary conditions at 300 K. Intermolecular van der Waals interactions were calculated with a cutoff of 12 Å (switching function starting at 10 Å). Long-range electrostatic forces were calculated using the Particle mesh Ewald (PME) summation method. The Langevin thermostat was used to maintain a constant temperature in the NVT ensemble. The elementary cell extension of the system was 115×115×115 Å where the periodicity along the z-axis was increased deliberately to create 95 Å of empty space above the surface. To keep the amorphous slab rigid, silica atoms were fixed at their minimized positions during the MD simulation.

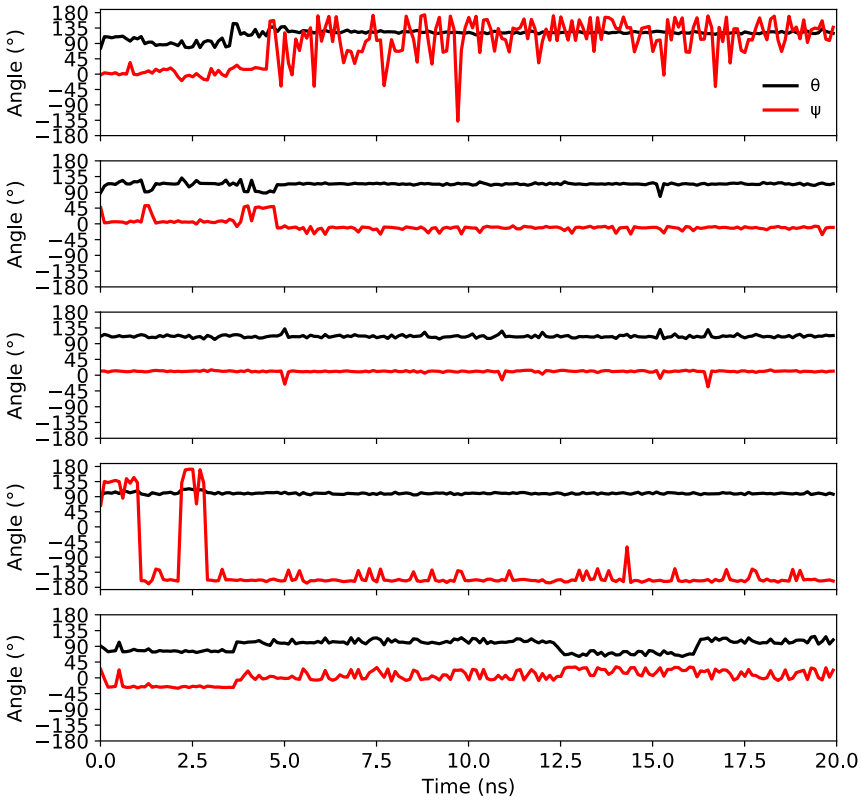

Figure S5. Time evolution of the Euler tilt (θ) and twist (ψ) angles describing the orientation of the carbaryl's aromatic ring with respect to the silica surface (see main text). Each panel correspond to five selected individual molecules. Note that carbaryl molecules rarely changes the original orientation (we remark that ψ=±180° correspond to the same orientation)`.

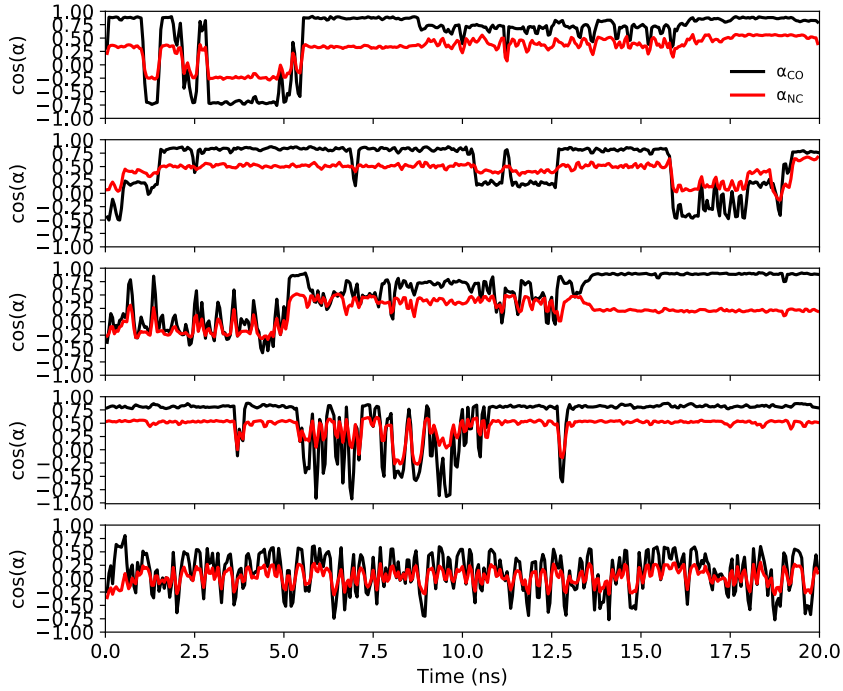

Figure S6. Time evolution of the (cosine of) angles describing orientation of the carbonyl C=O bond vector (α_{CO}) and N-CH_3 bond vector (α_{NC}) with respect to the silica surface (see main text). Each panel correspond to five selected individual molecules. Note that carbaryl molecules explore the rough silica surface with no preferential orientation until an energetically favorable anchoring site is found that tightly bound the pesticide to the interface for several ns.

DFT-based SFG spectra

DFT Calculations

Molecular geometry optimizations at the DFT level were performed with the Gaussian 16 software package,[19] using the B3LYP hybrid functional[14] and the 6-31+G(d) basis set.[15, 16] Harmonic frequency calculations were performed on the optimized stationary points to obtain frequencies, dipole and polarizability derivatives for each normal mode. An "ultrafine" integration grid (99 radial shells and 590 angular points per shell) was used for the frequency calculations to obtain accurate results. Additionally, anharmonic frequency calculations based on second-order perturbation theory (VPT2)[20-23] were performed to obtain coupling parameters for the inclusion of Fermi resonances (FR). All harmonic frequencies were scaled by 0.955 to facilitate the comparison with experimental spectra.

SFG spectra were simulated at the DFT level as has been previously described. [4, 24-33] Briefly, we computed the second-order molecular hyperpolarizabilities,

$$\beta_{\alpha\beta\gamma,q} \approx \frac{\partial \alpha_{\alpha\beta}}{\partial Q_q}\frac{\partial \mu_\gamma}{\partial Q_q} \tag{S4}$$

where $\alpha_{\alpha\beta}$ and μ_γ are elements of the polarizability and dipole moment in the molecular frame, and Q_q is the normal mode coordinate of the q-th vibrational mode. The hyperpolarizability was then rotated to the laboratory frame to obtain the second-order susceptibility,

$$\chi^{(2)}_{ijk,q} = \sum_{\alpha\beta\gamma}\langle R(\psi)R(\theta)R(\phi)\beta_{\alpha\beta\gamma,q}\rangle \tag{S5}$$

where $R(\psi)$, $R(\theta)$, and $R(\phi)$ represent the Euler rotation matrices required to superimpose the axes of the molecular coordinate system with those of the macroscopic laboratory coordinate system. The orientation parameters, represented by the Euler angles ψ, θ, and φ, are defined by the angular displacement of each axis of the molecular coordinate system from the corresponding axis of the laboratory coordinate system. Angular brackets in equation (S5) represent averages over different configurations sampled from MD simulations. The SFG intensity was then computed, as follows:

$$I_{SFG}(\omega_{IR}) = \left|\sum_k \frac{\chi^{(2)}_{eff,q}}{\omega_{IR}-\omega_q+i\Gamma_q}\right|^2 \tag{S6}$$

where Γ_q= 15 cm^{-1} and the effective susceptibilities for SSP and PPP polarization are

$$\begin{gathered}\chi^{eff}_{ssp,q} = L_{yyz}\chi^{(2)}_{yyz,q}, \\ \chi^{eff}_{ppp,q} = L_{zxx}\chi^{(2)}_{zxx,q} + L_{zzz}\chi^{(2)}_{zzz,q} - L_{xxz}\chi^{(2)}_{xxz,q} - L_{xzx}\chi^{(2)}_{xzx,q}\end{gathered} \tag{S7}$$

where the L_{ijk} terms are the Fresnel factors (listed in **Table S4**) that depend on the refractive index of the interface as well as the incident angle of the beams.[34-36]

Table S4. Relevant Fresnel factors for SSP and PPP SFG simulation.[(a)]

Fresnel factor	Value
L_{zzz}	0.047
L_{zxx}	0.098
L_{xzx}	0.092
L_{xxz}	0.137
L_{yyz}	0.161

(a) The refractive index of the interfacial layer is assumed to be 1.465 and the refractive index of air and silica was taken to be 1 and 1.52, respectively.[36, 37]

DFT Frequencies

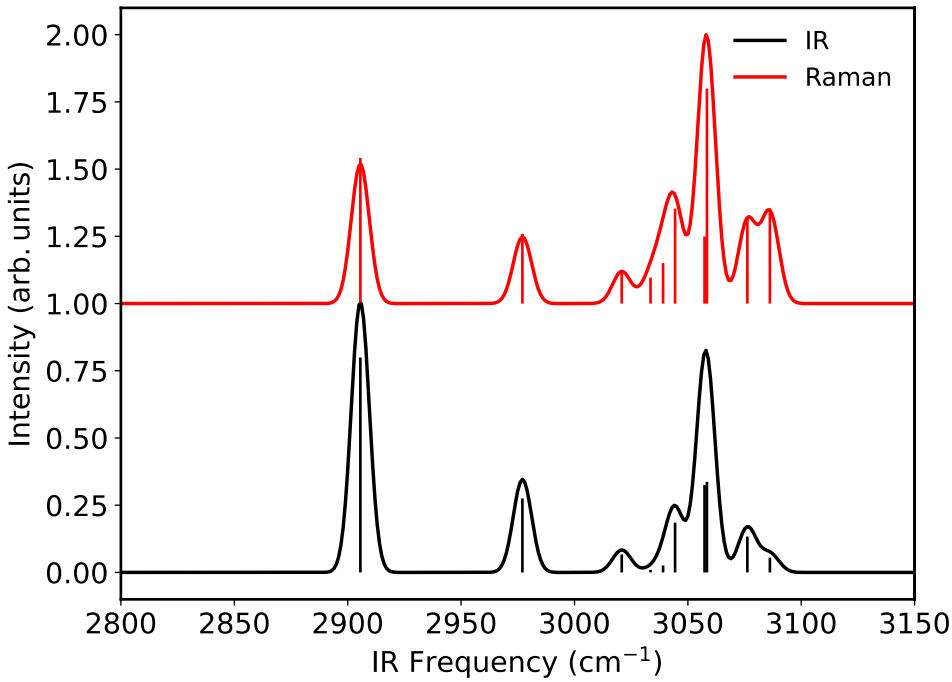

Figure S7. DFT harmonic Raman and IR spectra of carbaryl.

Table S5. Scaled harmonic DFT frequencies and mode assignment for carbaryl.

Frequency (cm^{-1})	Mode Assignment
2905.6	CH_3 (s)
2977.1	CH_3 (as)
3020.8	
3033.5	Aromatic CH
3039.1	
3044.4	
3057.3	
3058.4	
3076.2	
3086.2	

Fermi Resonances

To analyze the contribution of Fermi resonances to the C-H stretch spectral region, we simulated SFG spectra of carbaryl by including couplings between fundamental modes and combination and overtone bands using an effective Hamiltonian.[4, 38-40] Coupling parameters were obtained from anharmonic frequency calculations based on second-order perturbation theory (VPT2),[21, 22, 41] whereas frequencies of the fundamental, combination and overtone vibrational modes were computed at the harmonic level.

Figure S8 shows the SSP SFG spectra of carbaryl for the most likely carbaryl conformation. Note that the inclusion of anharmonic coupling splits the low frequency peak, corresponding to the CH3 (s) mode, giving rise to peaks centered at ~2863 cm^{-1} and ~2957 cm^{-1}. We remark that the anharmonic coupling also affects the shoulder appearing at ~3020 cm^{-1}.

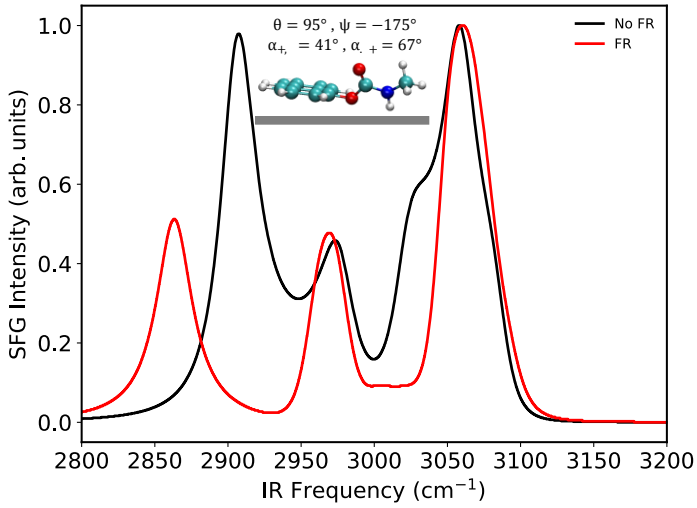

Figure S8. SSP SFG spectra of carbaryl in the C-H stretching region with (red line) and without (black line) accounting for Fermi resonances (FR). Note the splitting of the low frequency CH_3 (s) peak. A schematic of the orientation is shown in the inset.

Orientational dependence of SFG spectra

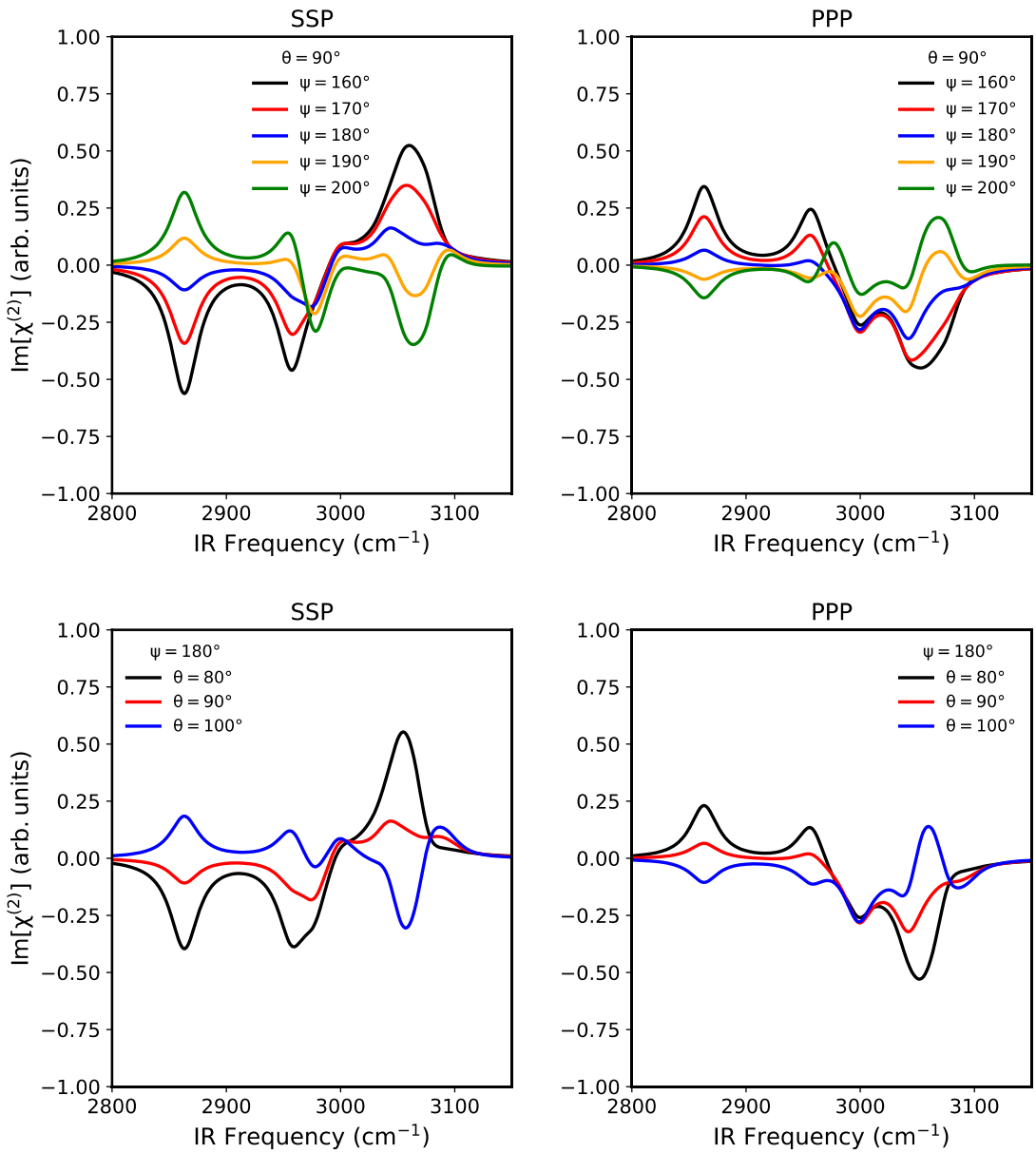

Figure S9. Dependence of the SFG spectra of carbaryl on the orientation of the phenyl ring with respect to the silica surface. We remark that a conformation with ($\theta = 90°, \psi = 0°$) represents a perfectly flat-lying ring. See Figure S8 for a schematic of the orientation.

References

(1) Fu, L.; Chen, S.-L.; Wang, H.-F. Validation of Spectra and Phase in Sub-1 cm^{-1} Resolution Sum-Frequency Generation Vibrational Spectroscopy through Internal Heterodyne Phase-Resolved Measurement. *J. Phys. Chem. B* **2016**, *120*, 1579-1589.

(2) Hu, X.-H.; Wei, F.; Wang, H.; Wang, H.-F. α-quartz crystal as absolute intensity and phase standard in sum-frequency generation vibrational spectroscopy. *J. Phys. Chem. C* **2019**, *123*, 15071-15086.

(3) Chase, H. M.; Ho, J.; Upshur, M. A.; Thomson, R. J.; Batista, V. S.; Geiger, F. M. Unanticipated Stickiness of α-Pinene. *J. Phys. Chem. A* **2017**, *121*, 3239-3246.

(4) Ho, J.; Psciuk, B. T.; Chase, H. M.; Rudshteyn, B.; Upshur, M. A.; Fu, L.; Thomson, R. J.; Wang, H.-F.; Geiger, F. M.; Batista, V. S. Sum Frequency Generation Spectroscopy and Molecular Dynamics Simulations Reveal a Rotationally Fluid Adsorption State of α-Pinene on Silica. *J. Phys. Chem. C* **2016**, *120*, 12578-12589.

(5) Cruz-Chu, E. R.; Aksimentiev, A.; Schulten, K. Water–Silica Force Field for Simulating Nanodevices. *J. Phys. Chem. B* **2006**, *110*, 21497-21508.

(6) Zhuravlev, L. T. The surface chemistry of amorphous silica. Zhuravlev model. *Colloids Surf., A* **2000**, *173*, 1-38.

(7) Leroch, S.; Wendland, M. Simulation of Forces between Humid Amorphous Silica Surfaces: A Comparison of Empirical Atomistic Force Fields. *J. Phys. Chem. C* **2012**, *116*, 26247-26261.

(8) Skelton, A. A.; Fenter, P.; Kubicki, J. D.; Wesolowski, D. J.; Cummings, P. T. Simulations of the Quartz(10$\bar{1}$1)/Water Interface: A Comparison of Classical Force Fields, Ab Initio Molecular Dynamics, and X-ray Reflectivity Experiments. *J. Phys. Chem. C* **2011**, *115*, 2076-2088.

(9) Lorenz, C. D.; Crozier, P. S.; Anderson, J. A.; Travesset, A. Molecular Dynamics of Ionic Transport and Electrokinetic Effects in Realistic Silica Channels. *J. Phys. Chem. C* **2008**, *112*, 10222-10232.

(10) Yesselman, J. D.; Price, D. J.; Knight, J. L.; Brooks Iii, C. L. MATCH: An atom-typing toolset for molecular mechanics force fields. *J. Comput. Chem.* **2012**, *33*, 189-202.

(11) Vanommeslaeghe, K.; Hatcher, E.; Acharya, C.; Kundu, S.; Zhong, S.; Shim, J.; Darian, E.; Guvench, O.; Lopes, P.; Vorobyov, I.; et al. CHARMM general force field: A force field for drug-like molecules compatible with the CHARMM all-atom additive biological force fields. *J. Comput. Chem.* **2010**, *31*, 671-690.

(12) Vanommeslaeghe, K.; MacKerell, A. D. Automation of the CHARMM General Force Field (CGenFF) I: Bond Perception and Atom Typing. *J. Chem. Inf. Model.* **2012**, *52*, 3144-3154.

(13) Vanommeslaeghe, K.; Raman, E. P.; MacKerell, A. D. Automation of the CHARMM General Force Field (CGenFF) II: Assignment of Bonded Parameters and Partial Atomic Charges. *J. Chem. Inf. Model.* **2012**, *52*, 3155-3168.

(14) Becke, A. D. Density-functional thermochemistry. III. The role of exact exchange. *J. Chem. Phys.* **1993**, *98*, 5648-5652.

(15) Frisch, M. J.; Pople, J. A.; Binkley, J. S. Self-consistent molecular orbital methods 25. Supplementary functions for Gaussian basis sets. *J. Chem. Phys.* **1984**, *80*, 3265-3269.

(16) Hariharan, P. C.; Pople, J. A. The influence of polarization functions on molecular orbital hydrogenation energies. *Theor. Chim. Acta* **1973**, *28*, 213-222.

(17) Phillips, J. C.; Braun, R.; Wang, W.; Gumbart, J.; Tajkhorshid, E.; Villa, E.; Chipot, C.; Skeel, R. D.; Kalé, L.; Schulten, K. Scalable molecular dynamics with NAMD. *J. Comput. Chem.* **2005**, *26*, 1781-1802.
(18) Martínez, L.; Andrade, R.; Birgin, E. G.; Martínez, J. M. PACKMOL: A package for building initial configurations for molecular dynamics simulations. *J. Comput. Chem.* **2009**, *30*, 2157-2164.
(19) Frisch, M. J.; Trucks, G. W.; Schlegel, H. B.; Scuseria, G. E.; Robb, M. A.; Cheeseman, J. R.; Scalmani, G.; Barone, V.; Petersson, G. A.; Nakatsuji, H.; et al. Gaussian 09, rev. D.01: Gaussian, I., Wallingford CT, 2016.
(20) Barone, V.; Bloino, J.; Guido, C. A.; Lipparini, F. A fully automated implementation of VPT2 Infrared intensities. *Chem. Phys. Lett.* **2010**, *496*, 157-161.
(21) Biczysko, M.; Bloino, J.; Carnimeo, I.; Panek, P.; Barone, V. Fully ab initio IR spectra for complex molecular systems from perturbative vibrational approaches: Glycine as a test case. *J. Mol. Struct.* **2012**, *1009*, 74-82.
(22) Bloino, J.; Barone, V. A second-order perturbation theory route to vibrational averages and transition properties of molecules: General formulation and application to infrared and vibrational circular dichroism spectroscopies. *J. Chem. Phys.* **2012**, *136*, 124108.
(23) Yagi, K.; Hirata, S.; Hirao, K. Vibrational quasi-degenerate perturbation theory: applications to fermi resonance in CO_2, H_2CO, and C_6H_6. *Phys. Chem. Chem. Phys.* **2008**, *10*, 1781-1788.
(24) Anfuso, C. L.; Snoeberger, R. C.; Ricks, A. M.; Liu, W.; Xiao, D.; Batista, V. S.; Lian, T. Covalent Attachment of a Rhenium Bipyridyl CO_2 Reduction Catalyst to Rutile TiO_2. *J. Am. Chem. Soc.* **2011**, *133*, 6922-6925.
(25) Anfuso, C. L.; Xiao, D.; Ricks, A. M.; Negre, C. F. A.; Batista, V. S.; Lian, T. Orientation of a Series of CO2 Reduction Catalysts on Single Crystal TiO_2 Probed by Phase-Sensitive Vibrational Sum Frequency Generation Spectroscopy (PS-VSFG). *J. Phys. Chem. C* **2012**, *116*, 24107-24114.
(26) Cattaneo, M.; Guo, F.; Kelly, H. R.; Videla, P. E.; Kiefer, L.; Gebre, S.; Ge, A.; Liu, Q.; Wu, S.; Lian, T.; et al. Robust Binding of Disulfide-Substituted Rhenium Bipyridyl Complexes for CO_2 Reduction on Gold Electrodes. *Front. Chem.* **2020**, *8*, 86.
(27) Clark, M. L.; Ge, A.; Videla, P. E.; Rudshteyn, B.; Miller, C. J.; Song, J.; Batista, V. S.; Lian, T.; Kubiak, C. P. CO_2 Reduction Catalysts on Gold Electrode Surfaces Influenced by Large Electric Fields. *J. Am. Chem. Soc.* **2018**, *140*, 17643-17655.
(28) Clark, M. L.; Rudshteyn, B.; Ge, A.; Chabolla, S. A.; Machan, C. W.; Psciuk, B. T.; Song, J.; Canzi, G.; Lian, T.; Batista, V. S.; et al. Orientation of Cyano-Substituted Bipyridine Re(I) fac-Tricarbonyl Electrocatalysts Bound to Conducting Au Surfaces. *J. Phys. Chem. C* **2016**, *120*, 1657-1665.
(29) Ge, A.; Rudshteyn, B.; Psciuk, B. T.; Xiao, D.; Song, J.; Anfuso, C. L.; Ricks, A. M.; Batista, V. S.; Lian, T. Surface-Induced Anisotropic Binding of a Rhenium CO_2-Reduction Catalyst on Rutile TiO2(110) Surfaces. *J. Phys. Chem. C* **2016**, *120*, 20970-20977.
(30) Ge, A.; Rudshteyn, B.; Videla, P. E.; Miller, C. J.; Kubiak, C. P.; Batista, V. S.; Lian, T. Heterogenized Molecular Catalysts: Vibrational Sum-Frequency Spectroscopic, Electrochemical, and Theoretical Investigations. *Acc. Chem. Res.* **2019**, *52*, 1289-1300.
(31) Ge, A.; Videla, P. E.; Lee, G. L.; Rudshteyn, B.; Song, J.; Kubiak, C. P.; Batista, V. S.; Lian, T. Interfacial Structure and Electric Field Probed by in Situ Electrochemical Vibrational Stark Effect Spectroscopy and Computational Modeling. *J. Phys. Chem. C* **2017**, *121*, 18674-18682.

(32) Ge, A.; Videla, P. E.; Rudshteyn, B.; Liu, Q.; Batista, V. S.; Lian, T. Dopant-Dependent SFG Response of Rhenium CO_2 Reduction Catalysts Chemisorbed on $SrTiO_3$ (100) Single Crystals. *J. Phys. Chem. C* **2018**, *122*, 13944-13952.
(33) Mifflin, A. L.; Velarde, L.; Ho, J.; Psciuk, B. T.; Negre, C. F. A.; Ebben, C. J.; Upshur, M. A.; Lu, Z.; Strick, B. L.; Thomson, R. J.; et al. Accurate Line Shapes from Sub-1 cm^{-1} Resolution Sum Frequency Generation Vibrational Spectroscopy of α-Pinene at Room Temperature. *J. Phys. Chem. A* **2015**, *119*, 1292-1302.
(34) Wang , H.-F.; Gan, W.; Lu, R.; Rao, Y.; Wu, B.-H. Quantitative spectral and orientational analysis in surface sum frequency generation vibrational spectroscopy (SFG-VS). *Int. Rev. Phys. Chem.* **2005**, *24*, 191-256.
(35) Yan, E. C. Y.; Fu, L.; Wang, Z.; Liu, W. Biological Macromolecules at Interfaces Probed by Chiral Vibrational Sum Frequency Generation Spectroscopy. *Chem. Rev.* **2014**, *114*, 8471-8498.
(36) Zhuang, X.; Miranda, P. B.; Kim, D.; Shen, Y. R. Mapping molecular orientation and conformation at interfaces by surface nonlinear optics. *Phys. Rev. B* **1999**, *59*, 12632-12640.
(37) Wang, H.-F.; Velarde, L.; Gan, W.; Fu, L. Quantitative Sum-Frequency Generation Vibrational Spectroscopy of Molecular Surfaces and Interfaces: Lineshape, Polarization, and Orientation. *Annu. Rev. Phys. Chem.* **2015**, *66*, 189-216.
(38) Guo, Z.; Zheng, W.; Hamoudi, H.; Dablemont, C.; Esaulov, V.; Bourguignon, B. On the chain length dependence of CH_3 vibrational mode relative intensities in sum frequency generation spectra of self assembled alkanethiols. *Surf. Sci.* **2008**, *602*, 3551-3559.
(39) Jetzki, M.; Luckhaus, D.; Signorell, R. Fermi resonance and conformation in glycolaldehyde particles. *Can. J. Chem.* **2004**, *82*, 915-924.
(40) Perets, E. A.; Videla, P. E.; Yan, E. C.; Batista, V. S. Chiral inversion of amino acids in antiparallel β-sheets at interfaces probed by vibrational sum frequency generation spectroscopy. *J. Phys. Chem. B* **2019**, *123*, 5769-5781.
(41) Barone, V.; Bloino, J.; Guido, C. A.; Lipparini, F. A fully automated implementation of VPT2 Infrared intensities. *Chem. Phys. Lett.* **2010**, *496*, 157-161.